RESEARCH ARTICLE | OCTOBER 31 2024

MHD-induced beta limits in the Large Helical Device

A. M. Wright ; N. M. Ferraro

Phys. Plasmas 31, 102509 (2024)
https://doi.org/10.1063/5.0228667

Physics of Plasmas ARTICLE pubs.aip.org/aip/pop

MHD-induced beta limits in the Large Helical Device

Cite as: Phys. Plasmas **31**, 102509 (2024); doi: 10.1063/5.0228667
Submitted: 14 July 2024 · Accepted: 10 October 2024 ·
Published Online: 31 October 2024

A. M. Wright[1,a)] and N. M. Ferraro[2]

AFFILIATIONS

[1]University of Wisconsin–Madison, Madison, Wisconsin 53706, USA
[2]Princeton Plasma Physics Laboratory, Princeton, New Jersey 08543, USA

[a)]Author to whom correspondence should be addressed: adelle.wright@wisc.edu

ABSTRACT

Using the extended-magnetohydrodynamics code, M3D-C1, we perform a systematic numerical study of the effect of externally applied heating on the achievable plasma beta in a ten field-period heliotron. Heat sources of varying intensity are applied to a vacuum magnetic field that is representative of the standard configuration of the Large Helical Device, with $R_0 = 3.66$ m, where R_0 is the radial position of the magnetic axis in vacuum. As the system is driven to a state that is unstable to low-n magnetohydrodynamic (MHD) modes, nonlinear mode interactions lead to the formation of chaotic magnetic fields. With sufficiently strong heating, a collapse of the electron temperature profile is observed. This demonstrates the necessity of simulating the self-consistent evolution of plasma profiles, without imposing assumptions on the structure of the magnetic field, to accurately determine transport properties in stellarator plasmas. It also highlights the value of these advanced simulation capabilities for accelerating the development of high-performance stellarator operating scenarios.

I. INTRODUCTION

In stellarators, the confining magnetic field is produced predominantly through geometric effects by allowing non-axisymmetric variations in the plasma shape. Unlike tokamaks, stellarators do not require externally driven toroidal current to produce confinement. While it is not true that all stellarators have no net toroidal current, the net current carried is much lower than for typical tokamaks. As a result, stellarator plasmas can exhibit greater intrinsic stability to macroscopic, magnetohydrodynamic (MHD) instabilities.[1]

In magnetically confined fusion plasmas, heat transport is strongly anisotropic. Heat conduction parallel to the magnetic field $\boldsymbol{B}(\boldsymbol{x})$ is much stronger than transport in the direction perpendicular to it. For typical fusion-relevant tokamak and stellarator plasmas, the difference is between $O(10^6)$ and $O(10^8)$. Consequently, the structure of the magnetic field is a key determinant of the heat transport properties in these plasmas. For example, outward radial transport of heat will be very different in a chaotic magnetic field than in one with continuously nested magnetic surfaces. In the former, magnetic field lines fill a finite three-dimensional (3D) volume. In the latter, magnetic field lines lie on two-dimensional surfaces.

Non-axisymmetric, i.e., 3D, magnetic fields can admit a variety of structures that are not present in axisymmetric fields. These structures, which include magnetic islands and chaotic magnetic fields, can significantly modify the transport properties of fusion plasmas. Since stellarator magnetic fields are intrinsically 3D, determining the self-consistent evolution of the magnetic field in the presence of dissipation and evolving plasma profiles is essential for accurately evaluating transport characteristics.

Nonlinear interactions between MHD instabilities are a well-known mechanism for changing magnetic field structure. This may be due to overlap of magnetic islands[2] or disordering of magnetic field lines due to mixing of the plasma fluid that is induced by the growth of MHD instabilities. Consequently, the nonlinear characteristics of MHD instabilities, such as saturation amplitude, can strongly influence these changes. In this respect, the observed differences in the nonlinear MHD stability characteristics of stellarators compared to tokamaks are an important open question to address.[3] Non-axisymmetric machines, such as the Large Helical Device (LHD),[1] have been able to significantly exceed linear MHD stability thresholds, without significant degradation of plasma performance.[4]

Understanding how MHD instabilities lead to changes in magnetic field structure and examining the resultant impact on heat transport requires self-consistently modeling the nonlinear evolution of the magnetic field, temperature profiles as well as other fluid variables. In stellarators, this is an extremely challenging numerical problem, for which there exist only a handful of tools with such capabilities. In this work, we use the extend-MHD code, M3D-C1,[5] to study how MHD instabilities, driven by an external heat source, modify magnetic field structure, and impact confinement in a representative LHD plasma configuration.

In Sec. II, we describe numerical parameters and simulation tools. In Sec. III, we present the results of the computationally intensive, systematic study. Finally, discussion and conclusions are described in Sec. IV.

II. METHODS

In this study, we investigate how the nonlinear evolution of long wavelength MHD instabilities affects the maximum plasma beta that can be maintained, given a fixed external heating source. Each simulation is initialized with the same vacuum magnetic field, which is calculated from the coil geometry of the Large Helical Device (LHD).[1] The radial position of the magnetic axis in vacuum is $R_0 = 3.66\,\mathrm{m}$ at $\phi = 18^\circ$, the on-axis magnetic field is $\approx 3\,\mathrm{T}$ and the average minor radius is $a = 0.56\,\mathrm{m}$. A Poincaré section of the vacuum magnetic field is shown in Fig. 1. The corresponding rotational transform is shown in Fig. 2. These vacuum parameters are representative of the so-called standard discharge, where the plasma is considered to be neither "inward" nor "outward" shifted.[6]

The external heating is modeled by a heat source that is constant in time. The radial profile is a Gaussian centered at the initial position of the magnetic axis, with variance 0.4Ψ, where Ψ is the normalized toroidal flux. For each simulation, the amplitude and deposition location of the heat source do not vary in time. Consequently, as the position of the magnetic axis changes due to the Shafranov shift at finite plasma pressure, the heat source is no longer centered on-axis. However, because the heating profile used in this study is quite broad, even compared to the shift of the magnetic axis, we do not anticipate a significant impact on this study. In the experiment, the heat deposition location is generally fixed. For a narrower heat source, it may be that the current approach would not be suitable. The amplitude of the heat source is the parameter that is varied for this parametric study. Experimentally, plasmas heated from the vacuum magnetic field conditions considered in this work are routinely observed to have significant low-n MHD mode activity at some finite plasma beta, β.[8,9] Specifically, $n = 1, 2, 3$ modes are observed.[4,8] Here, n is the toroidal Fourier mode number and β is the ratio of the plasma to magnetic pressure and discussed further as follows. However, in this part of the LHD operational space, it has been well established that there is no large-scale loss of confinement, even though the plasma is linearly unstable to MHD modes.[8]

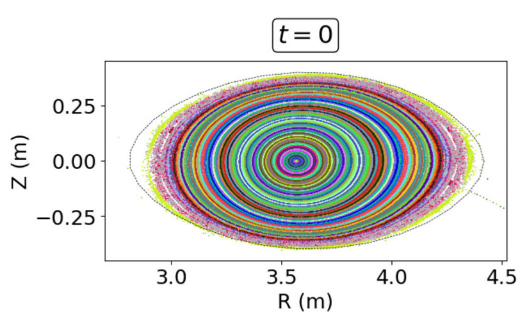

FIG. 1. Poincaré section ($\phi = 18^\circ$) of the vacuum magnetic field used in this study. The black dotted line indicates the plasma boundary that would be calculated by the VMEC code.[7]

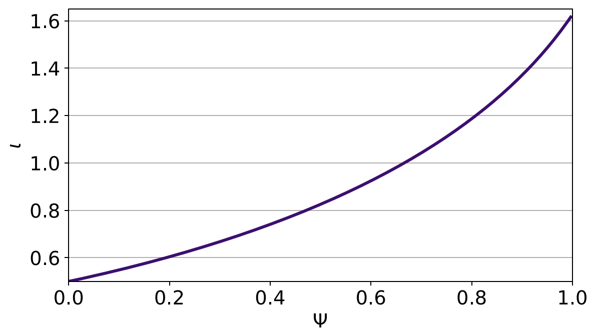

FIG. 2. Rotational transform profile for the vacuum magnetic field, as calculated by VMEC, with $R_0 = 3.66\,\mathrm{m}$.

Within the literature, several different definitions of plasma β are used to describe the properties of LHD plasmas.[4] In practice, identifying what constitutes the "edge" of the plasma in LHD is non-trivial because the magnetic field is typically non-integrable. This makes a standardized measure of β difficult to obtain. Throughout this work, we use a volume-averaged measure of β, denoted $\langle\beta\rangle_{\mathrm{M3D-C1}}$, which is obtained by averaging over the entire computational domain. In the simulations, the plasma is spatially separated from the edge of the computational domain by a vacuum region. This allows the plasma shape and edge magnetic field structure to be modeled self-consistently. As a consequence, the area over which $\langle\beta\rangle_{\mathrm{M3D-C1}}$ is being calculated is larger than the plasma volume. This leads to values of β that are lower than what is typically quoted elsewhere, see Ohdachi *et al.*[9] and Yamada,[10] for example.

We use the extended-MHD code, M3D-C1,[5,11] to perform a systematic study of the effect of plasma heating, and induced MHD instabilities, on the maximum maintainable plasma beta. Here, we define the "maximum maintainable plasma beta" as the maximum value of β that can be sustained without a major collapse in the plasma temperature or density profiles. In total, we consider ten different values for the amplitude of the external heating source. The radial profile for each source is shown in Fig. 3. We define a heating ratio which is the heat source divided by $\kappa_\perp$, the perpendicular heat conductivity coefficient. The heating ratio accounts for the fact that we use a larger-than-physical value of $\kappa_\perp$. As will be discussed in Sec. II A, this is to keep

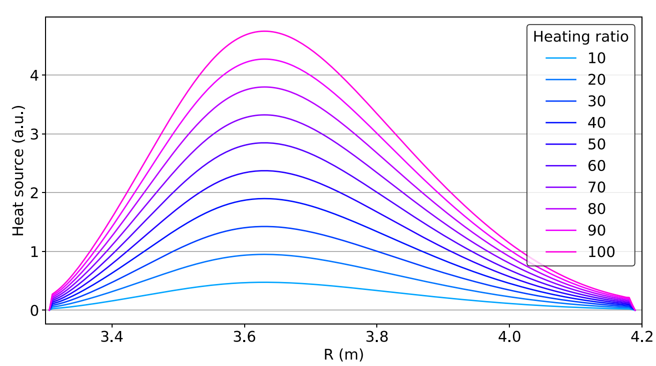

FIG. 3. Radial profiles of the heating sources considered in the study, shown at $\phi = 18^\circ$. Here, "heating ratio" measures the relative amplitude of each source.

the total wall-clock time manageable. For completeness; the maximum available heating power in LHD is ~ 23 MW.[10]

M3D-C1 is a finite element code that uses a split-implicit time-stepping algorithm. The elements are C^1-continuous, unstructured triangles in the poloidal plane and extruded toroidally using Hermite-cubic bases. An example of a stellarator mesh may be found in Fig. 1 of Zhou *et al.*[11] For stellarator applications, we emphasize two key properties. First, M3D-C1 does not use spectral bases. This distinguishes it from other nonlinear stellarator MHD codes, such as JOREK,[12] NIMSTELL,[13] and MIPS.[14] Second, the discretization is independent of the magnetic field or plasma properties. This makes M3D-C1 effective at capturing complex evolution of the magnetic field structure, such as the breakup of magnetic surfaces and formation of chaotic magnetic fields and magnetic islands. For the simulations presented, the computational domain is fully non-axisymmetric. We use 4.8×10^5 elements, corresponding to 40 toroidal planes. The requisite toroidal resolution was determined by convergence studies.

In line with current practice,[11,15,16] the computational domain for this study is conformal to the vacuum plasma shape. We emphasize, however, that the code is not limited to such a representation. Here, we set the boundary of the computational domain to be separated from the plasma edge so that the plasma being simulated is not wall-limited. Since this remains a single region calculation, the same model equations are being solved throughout the volume. So that we are able to model the self-consistent evolution of the plasma shape, the computational domain is 20% larger than the plasma volume.

For this work, we use a single-fluid, visco-resistive MHD model, the details of which are given in Jardin *et al.*[5] and have been restated in the Appendix for convenience. The plasma is assumed to be isothermal so that $T_i(\boldsymbol{x}, t) = T_e(\boldsymbol{x}, t)$, where T_i and T_e are the ion and electron temperatures, respectively. The system is closed by relating the heat flux density $\boldsymbol{q}(\boldsymbol{x}, t)$ to the electron temperature by

$$\boldsymbol{q}(\boldsymbol{x}, t) = -\kappa_\perp \nabla T_e(\boldsymbol{x}, t) - \kappa_\| \frac{\boldsymbol{B}(\boldsymbol{x}, t)\boldsymbol{B}(\boldsymbol{x}, t)}{B(\boldsymbol{x}, t)^2} \cdot \nabla T_e(\boldsymbol{x}, t). \quad (1)$$

Here, $\kappa_\perp$ and $\kappa_\|$ are the perpendicular and parallel heat conductivity coefficients, respectively, and $\boldsymbol{B}(\boldsymbol{x}, t)$ is the magnetic field. In place of advancing the pressure $p(\boldsymbol{x}, t)$, the electron temperature and number density $n(\boldsymbol{x}, t)$ are dynamic variables. The pressure can then be evaluated using $p(\boldsymbol{x}, t) = n(\boldsymbol{x}, t) T_e(\boldsymbol{x}, t)$.

A. Numerical resolution, dissipation, and transport parameters

Numerical studies that involve systematic scans over parameters of interest (in this case, external heating) can provide significant insight into the underlying physics of interest. Doing so can shed light on behavior that cannot be resolved by lower-fidelity reduced models, such as MHD equilibrium codes, which are commonly used in stellarator analysis.[17] However, numerical studies of the kind presented in this work require considerable computational resources, placing practical constraints on the scope and scale of such parametric studies. The challenge, then, is to balance these competing considerations. Namely, to simultaneously maximize the obtainable physics insights and the efficiency with which computational resources are expended. These considerations inform the choices for the toroidal resolution and perpendicular heat conductivity used in this work.

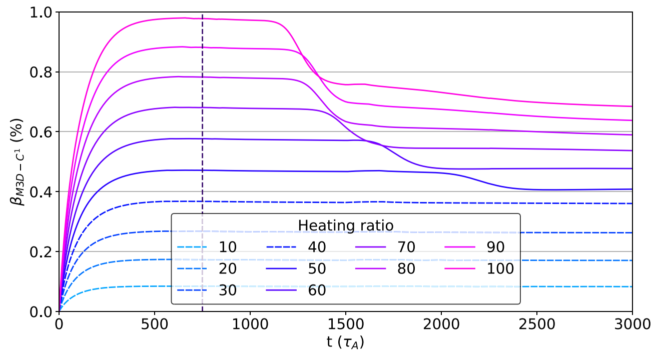

FIG. 4. Time evolution of $\langle\beta\rangle_{\mathrm{M3D-C1}}$ for each heating profile. Above a critical value (heating ratio >40), a sudden decrease in $\langle\beta\rangle_{\mathrm{M3D-C1}}$ is observed. The vertical dashed line indicates the time at which the saturated plasma beta is measured (see Fig. 5).

For each heating source, simulations are advanced in increments of $\Delta t = 5\tau_A$, where τ_A is the Alfvén time. The simulations are terminated at $t = 3000\tau_A$, which is sufficient to observe saturation of the plasma dynamics after a β limit is reached. The wall-clock time for each simulation is approximately 67 h, corresponding to 48 000 CPU-hours. Thus, the total computational cost for the simulations presented is approximately 4.8×10^5 CPU-hours and 28 days wall-clock time.

To ensure the resource requirements for this study remain feasible, each simulation uses 40 toroidal planes. This is sufficient to resolve the macroscopic plasma dynamics of interest, which are primarily determined by MHD instabilities with toroidal Fourier mode numbers $n = 1$ and $n = 2$. Since the mode numbers of interest are less than the periodicity of LHD (which has ten field periods), full torus simulations are performed. As a point of reference, this toroidal resolution is sufficient to resolve contributions to the plasma dynamics from toroidal Fourier modes with $n \leq 20$. Within each poloidal plane, the resolution we use is sufficient to resolve the mode structure of high-n ballooning modes.

For stellarator applications, an advantage of the M3D-C1 code is that it is able to model anisotropic heat transport in the presence of a self-consistently evolving magnetic field. For this work, we set $\kappa_\|/\kappa_\perp = 10^6$, which is realistic for LHD, where $\kappa_\perp$ is empirically inferred from anomalous diffusivity.[18] We set $\kappa_\perp = 10^{-4}$, which

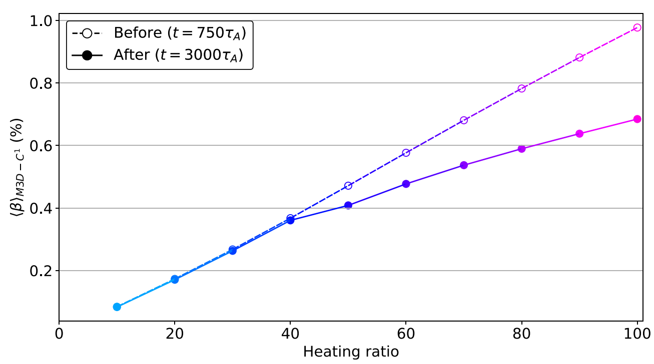

FIG. 5. Values of $\langle\beta\rangle_{\mathrm{M3D-C1}}$ as a function for heating ratio at $t = 750\,\tau_A$ (hollow circles) and $t = 3000\,\tau_A$ (filled circles). At heating ratio $= 40$, the two curves bifurcate. This coincides with onset of a sudden collapse in $\langle\beta\rangle_{\mathrm{M3D-C1}}$.

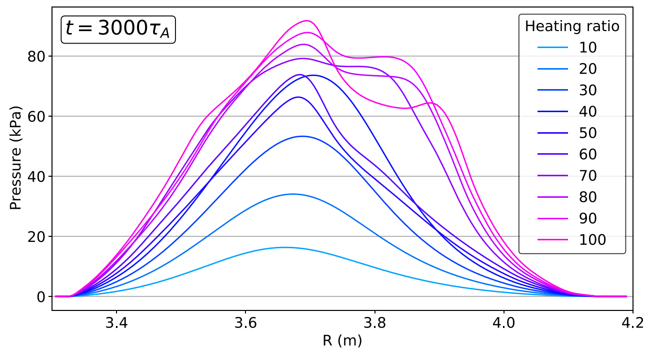

FIG. 6. Cross-sections ($\phi = 18^{\circ}$) of the plasma pressure profile taken at the end of the simulation ($t = 3000\tau_A$) as a function of heating ratio. As the applied heating increases, a clear change in the structure of the profile is observed.

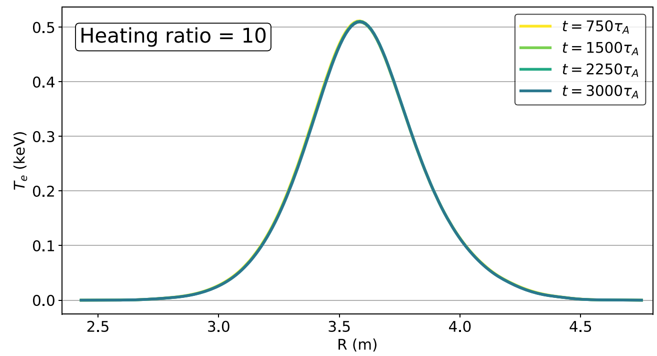

FIG. 7. Cross-sections ($\phi = 18^{\circ}$) of the electron temperature profile at different times, for heating ratio $= 10$. The profile remains peaked and essentially unchanged as a function of time.

corresponds to a perpendicular heat diffusivity of $\chi_\perp = 220\ \mathrm{m}^2/\mathrm{s}$. Our choice of $\chi_\perp$ is about one to two orders of magnitude larger than what is experimentally determined on LHD, depending on the confinement regime.[19] This, however, does not affect the qualitative conclusions of this study. The effect of increasing $\kappa_\perp$ is to decrease the pressure relaxation time since $\tau_{\mathrm{relaxation}} \sim a^2/\chi_\perp$ where $a = 0.56$ m is the minor radius of the equilibrium. For a given heating source, this accelerates the plasma heating, allowing the plasma beta to saturate more quickly in the simulations. Ultimately, this reduces the time that needs to be simulated by orders of magnitude. At the same time, however, we choose $\kappa_\perp$ so that there is still sufficient separation of timescales between the saturation of the plasma beta due to external heating, and the MHD dynamics of interest. The timescale for resistive MHD instabilities is the hybrid timescale, $\tau_{reconnection} = \tau_A^s \tau_R^{s-1}$ where $0 < s < 1$, τ_A is the Alfvén time, $\tau_R = \mu_0 a^2/\eta$ and η is the resistivity.[20] For the plasma conditions considered ($s > 0.5$), we do indeed see that $\tau_{reconnection} \ll \tau_{relaxation}$.

As with previous MHD simulations of LHD plasmas, this study uses a constant resistivity profile.[14,21,22] No hyper-dissipation parameters are used. We choose $\eta = 2.741 \times 10^{-7}\ \Omega\,\mathrm{m}$, which corresponds to a Lundquist number of $S = 10^7$. To allow for comparatively large time steps, an enhanced viscosity is chosen. We set $\nu = 1.824\ \times 10^{-3}\ \mathrm{kg\,m^{-1}\,s^{-1}}$, which is about 100 times higher than would be expected in practice. In previous studies of LHD plasmas with the MIPS code, enhanced viscosity was also used to improve numerical stability.[14] Increasing viscosity has the effect of reducing growth rates of high-n instabilities. The effect on the low-n modes of interest is not significant, which justifies the approach taken in this work.

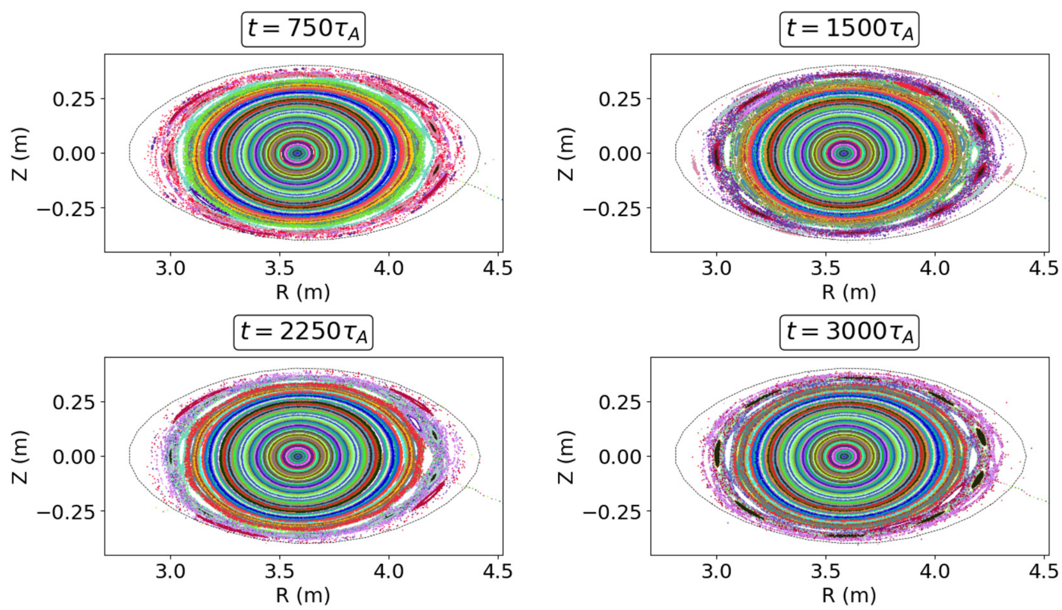

FIG. 8. Poincaré sections (at $\phi = 18^{\circ}$) of the magnetic field at four different times, for the heat ratio $= 10$ case, which shows very little change in the magnetic field structure.

III. RESULTS AND DISCUSSION

For the following discussion, we adopt $\langle\beta\rangle_{\mathrm{M3D\text{-}C1}}$ as the measure of the plasma β. As described in Sec. II, when the magnetic field at the plasma edge is chaotic, it becomes challenging to identify the plasma boundary. Without this, β averaged over the plasma volume cannot be obtained, as is the case in this work. Instead, as noted in Sec. II, we chose to average over the entire computational domain, which is larger than the plasma volume. Consequently, the β values subsequently shown are lower than what would be expected if the average was performed over the plasma volume. This is consistent with the fact that β limits observed on LHD are much higher than the values shown here.[9]

A. Exceeding the linear stability threshold

In Fig. 4, we plot $\langle\beta\rangle_{\mathrm{M3D\text{-}C1}}$ as a function of time for each heating profile considered. In all cases, the $\langle\beta\rangle_{\mathrm{M3D\text{-}C1}}$ saturates at $\sim 500\,\tau_A$. As the heating ratio increases, we observe a sudden decrease in the plasma beta (Fig. 4, solid lines). The magnitude of this drop increases with increasing heating ratio, while the onset timing decreases. For low values of the heating ratio (below 50), no such decrease in plasma beta is observed (Fig. 4, dashed lines).

In Fig. 5, we plot the values of $\langle\beta\rangle_{\mathrm{M3D\text{-}C1}}$ as a function of the heating ratio before ($t = 750\,\tau_A$, Fig. 4 vertical dashed line) and after ($t = 3000\,\tau_A$) the sudden decrease. When the heating ratio is 40, the two curves bifurcate as the applied heating drives the system past a linear stability boundary for an $n = 1$ interchange MHD mode. This instability is associated with the $\iota = 1/2$ magnetic surface, which is in the core of the plasma (see Fig. 2). Based on the vacuum magnetic axis, this is broadly consistent with what is observed in experiment (see Fig. 8 of Ref. 9).

In Fig. 6, we show pressure profiles, taken at the $Z = 0$ plane and the final time ($t = 3000\,\tau_A$) for each heating ratio considered. As expected, for lower heating ratios, the profiles are peaked around the magnetic axis. The maximum value increases with increasing applied heating. Above a critical value, however, we observe a qualitative change in the overall structure of the profiles, which become significantly flattened in the core.

B. Nonlinear interactions and profile changes

In the simulations, the density profiles are initially spatially uniform. While density is a dynamic variable, we do not find that the density profile changes significantly in time. Thus, the observed behaviors are due to changes in the temperature profile. These can be understood by considering three representative cases in greater detail.

The first case corresponds to a heating ratio of 10, which sits well below the $n = 1$ stability boundary. In Fig. 7, we plot cross-sections of the electron temperature profile at four different times. Once $\langle\beta\rangle_{\mathrm{M3D\text{-}C1}}$ has saturated, the profiles remain essentially unchanged. Similarly, the Poincaré sections shown in Fig. 8 show little change in the magnetic field structure.

By contrast, in Figs. 9 and 10 we show the evolution of the temperature profile for two cases above the stability boundary (heating ratio 50 and 80, respectively). Both profiles change considerably and also differ qualitatively from one another. For the heating ratio 50 case, there is a significant decrease in the central value of the temperature associated with the drop in $\langle\beta\rangle_{\mathrm{M3D\text{-}C1}}$. However, the profile remains centrally peaked. On the other hand, for the heating ratio 80 case, there is both a significant decrease in the central value of the temperature, and broad flattening of the profile, associated with the drop in $\langle\beta\rangle_{\mathrm{M3D\text{-}C1}}$.

As discussed in Sec. III A, the drop in $\langle\beta\rangle_{\mathrm{M3D\text{-}C1}}$ occurs due to growth of an $n = 1$ interchange mode. The flattening of the profiles—seen in Fig. 10 but not Fig. 9—occurs due to growth of a secondary $n = 2$ MHD instability. The latter is associated with the $\iota = 2/3$

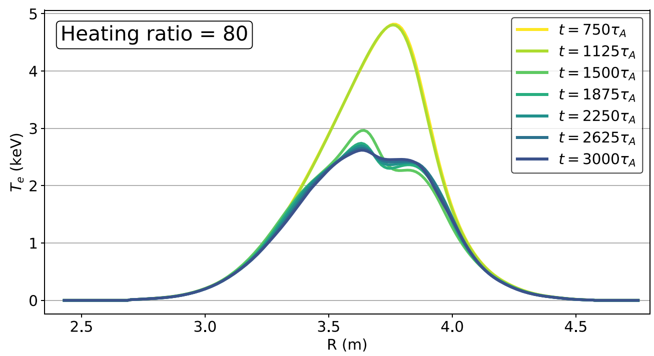

FIG. 10. Cross-sections ($\phi = 18^\circ$) of the electron temperature profile at different times, for heating ratio 80. Once the stability threshold is crossed, a significant broadening and decrease in the central profile is observed.

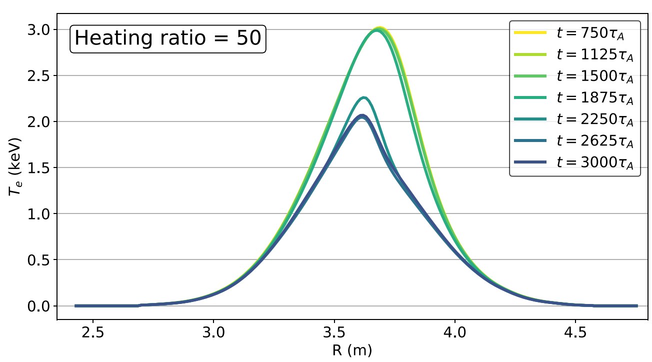

FIG. 9. Cross-sections ($\phi = 18^\circ$) of the electron temperature profile at different times, for heating ratio 50. While the profile remains peaked, the on-axis value decreases notably once the stability threshold is crossed.

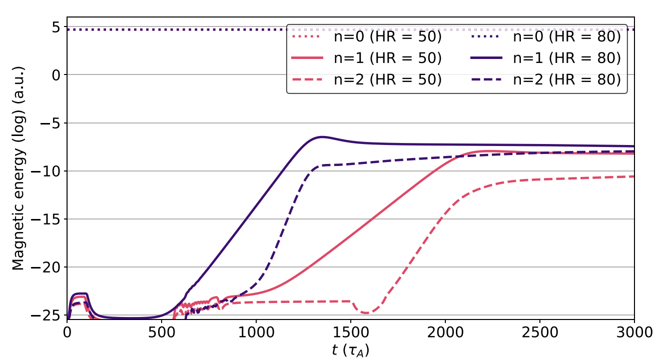

FIG. 11. Toroidal Fourier components of the magnetic energy for the heating ratio 50 (pink) and 80 (purple) cases. Namely, $n = 0$ (dotted line), $n = 1$ (solid line), and $n = 2$ (dashed line).

resonant surface, which is about halfway out in radius (see Fig. 2). The growth of this mode is driven when the heating is sufficiently strong.

In Fig. 11, we plot the $n = 0, 1, 2$ toroidal Fourier components of the magnetic energy, which are obtained *a posteriori* by Fourier transform. Comparing the saturated amplitudes of the $n = 1$ and $n = 2$ toroidal Fourier components, we see a marked difference between the two heating cases. In the case with smaller heating ratio, the two saturated amplitudes differ by several orders of magnitude. For the case with larger heating ratio, the saturated amplitudes become much more comparable to within the same order of magnitude. Crucially, this means that in the latter case, there is overlap in the perturbations associated with the primary and secondary instabilities, as illustrated in Fig. 12. The dynamics resulting from nonlinear interactions between these two modes leads to the rapid breakup of magnetic surfaces. As a consequence, a large volume of chaotic magnetic field forms in the core of the plasma. This is what causes the temperature collapse observed in Fig. 10.

IV. CONCLUSION

We have seen that mixing between strongly coupled modes, that is, modes with comparable saturated amplitudes, c.f. Fig. 11, can produce fast changes in the magnetic field structure. In this case, it led to breakup of magnetic surfaces and formation of chaotic magnetic fields that fill a significant fraction of the plasma volume, c.f. Fig. 12. Although a qualitative comparison, the low-n modes that drive the dynamics observed in this work are consistent with what is observed in LHD for the standard configuration.[4] In this part of the LHD configuration space, the simulation results suggest that low-n modes provide a mechanism that may constrain the achievable plasma β. Nonetheless, more quantitative comparisons and experimental validation are needed to draw firmer conclusions. What is known, however, is that LHD plasmas can operate in several distinct dynamical regimes.[9] The maximum plasma β may, therefore, be limited by a variety of mechanisms. For example, in the outward shifted configurations $R_0 > 3.75$ m, abrupt loss-of-confinement events are observed. These so-called core density collapse events appear to place a rigid limit on the maximum plasma β.[9] High-n MHD ballooning modes have been proposed as a possible cause of this phenomenon.[23,24] Combined, this motivates continued work on understanding the relationships between high-n and low-n MHD modes in setting β limits in LHD plasmas.

The difference in heat diffusivity parallel and perpendicular to a magnetic field line ($\kappa_{\parallel}/\kappa_{\perp}$) suggests that heat transport properties can be very different in a chaotic magnetic field compared to one with nested magnetic surfaces. Since a chaotic magnetic field line fills a finite volume, this may facilitate radial heat transport that is faster than transport across a magnetic surface with $\kappa_{\perp}$. Since nonlinear MHD interactions can produce changes in the magnetic field structure, these dynamics have the potential to impact predicted heat transport properties in stellarator plasmas. To quantify this, it is necessary to accurately evaluate the heat flux $\boldsymbol{q}$. While we currently do not have the functionality to evaluate $\boldsymbol{q}$ given in Eq. (1), it is being developed and will be available for future studies. This will enable quantitative analysis

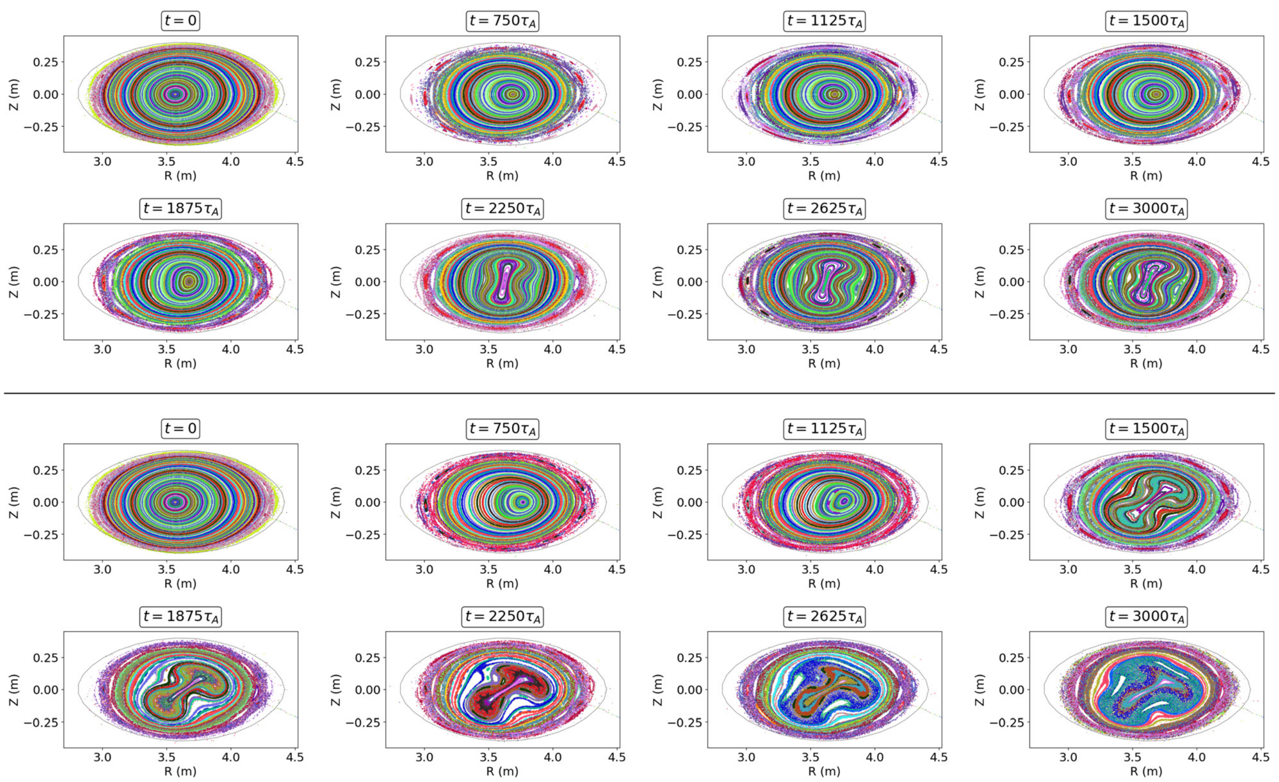

FIG. 12. Sequence of Poincaré sections of the magnetic field (taken at $\phi = 18^{\circ}$) as a function of time for the heating ratio 50 (top) and 80 (bottom) cases.

of the changes in transport properties due to magnetic field variations induced by nonlinear MHD dynamics.

We used the extended-MHD code, M3D-C1, to systematically study the effect of externally applied heating on the achievable plasma beta in a representative case of the so-called LHD standard configuration. By varying the strength of the applied heat source, we observed a transition from plasmas that are stable then unstable to an $n = 1$ core interchange mode. Continued heating fuels growth of a secondary $n = 2$ mode that is resonant halfway out in the plasma radius. With sufficiently strong heating, the two modes become strongly coupled (comparable saturated amplitudes), leading to nonlinear interactions that rapidly breakup magnetic surfaces in the plasma core. Eventually, this leads to a collapse of the electron temperature profile. This highlights the importance of being able to simulate fully nonlinear MHD dynamics with a self-consistently evolving magnetic field. Combined with a model that captures the key physics of strongly anisotropic heat transport in magnetically confined fusion plasmas, this allows for more accurate estimates of heat transport in stellarators by accounting for contributions due to MHD-induced changes to the magnetic field structure.

Very recently, there have been several studies which investigate nonlinear MHD in stellarators using reduced- and extended-MHD codes. This includes verification of the ideal-ballooning limit in Wendelstein 7-X[25] and β-limits in Wendelstein 7-AS.[26] These works also highlight the role of magnetic field structure in determining transport in stellarators and motivate the continued need for studies in this area.

ACKNOWLEDGMENTS

The authors gratefully acknowledge valuable discussions with Professor Y. Suzuki. This work was supported by the Department of Energy (Contract No. DE-AC02-09-CH11466) and the resources of the National Energy Research Scientific Computing Center (NERSC), Department of Energy Office of Science User Facility, through NERSC (Award No. FES-ERCAP0028267).

AUTHOR DECLARATIONS

Conflict of Interest

The authors have no conflicts to disclose.

Author Contributions

A. M. Wright: Conceptualization (lead); Data curation (lead); Formal analysis (lead); Funding acquisition (lead); Investigation (lead); Methodology (lead); Project administration (lead); Resources (lead); Software (lead); Validation (lead); Visualization (lead); Writing – original draft (lead). **N. M. Ferraro:** Formal analysis (supporting); Software (supporting); Supervision (equal); Writing – review & editing (equal).

DATA AVAILABILITY

The data that support the findings of this study are available from the corresponding author upon reasonable request.

APPENDIX: M3D-C1 MODEL EQUATIONS

The M3D-C1 equations used in this study are reproduced from Jardin *et al.*[5] as follows:

$$\frac{\partial n}{\partial t} + \nabla\cdot(n\boldsymbol{v}) = 0, \tag{A1}$$

$$nm_i\left(\frac{\partial \boldsymbol{v}}{\partial t} + \boldsymbol{v}\cdot\nabla\boldsymbol{v}\right) = \boldsymbol{J}\times\boldsymbol{B} - \nabla p - \nabla\cdot\Pi + \mathbf{F}, \tag{A2}$$

$$\frac{\partial p}{\partial t} + \boldsymbol{v}\cdot p + \gamma p\nabla\cdot v = (\gamma-1)\left[Q - \nabla\cdot\boldsymbol{q} + \eta J^2 - \boldsymbol{v}\cdot\mathbf{F} - \Pi:\nabla\boldsymbol{v}\right], \tag{A3}$$

$$\boldsymbol{J} = \frac{1}{\mu_0}\nabla\times\boldsymbol{B}, \tag{A4}$$

$$\frac{\partial \boldsymbol{B}}{\partial t} = -\nabla\times(\boldsymbol{v}\times\boldsymbol{B}) - \nabla\times(\eta\boldsymbol{J}), \tag{A5}$$

where n is the number density, $\boldsymbol{v}$ is the fluid velocity, m_i is the ion mass, $\boldsymbol{J}$ is the current density, $\boldsymbol{B}$ is the magnetic field, p is the pressure, Π is the viscous stress tensor, and $\mathbf{F}$ and Q denote external forces and heat sources, respectively. The adiabatic constant is $\gamma = 5/3$, η is the resistivity, $\boldsymbol{q}$ is the thermal heat flux, and μ_0 is the vacuum permeability.

REFERENCES

[1] A. Komori, H. Yamada, S. Imagawa, O. Kaneko, K. Kawahata, K. Mutoh, N. Ohyabu, Y. Takeiri, K. Ida, T. Mito *et al.*, "Goal and achievements of large helical device project," Fusion Sci. Technol. **58**, 1–11 (2010).
[2] B. V. Chirikov, "A universal instability of many-dimensional oscillator systems," Phys. Rep. **52**, 263–379 (1979).
[3] D. A. Gates, D. Anderson, S. Anderson, M. Zarnstorff, D. A. Spong, H. Weitzner, G. Neilson, D. Ruzic, D. Andruczyk, J. H. Harris *et al.*, "Stellarator research opportunities: A report of the national stellarator coordinating committee," J. Fusion Energy **37**, 51–94 (2018).
[4] S. Sakakibara, K. Watanabe, S. Ohdachi, Y. Narushima, K. Toi, K. Tanaka, K. Narihara, K. Ida, T. Tokuzawa, K. Kawahata *et al.*, "Study of MHD stability in LHD," Fusion Sci. Technol. **58**, 176–185 (2010).
[5] S. Jardin, N. Ferraro, J. Breslau, and J. Chen, "Multiple timescale calculations of sawteeth and other global macroscopic dynamics of tokamak plasmas," Comput. Sci. Disc. **5**, 014002 (2012).
[6] K. Watanabe, Y. Suzuki, S. Sakakibara, T. Yamaguchi, Y. Narushima, Y. Nakamura, K. Ida, N. Nakajima, H. Yamada, and L. E. Group, "Characteristics of MHD equilibrium and related issues on LHD," Fusion Sci. Technol. **58**, 160–175 (2010).
[7] S. Hirshman and O. Betancourt, "Preconditioned descent algorithm for rapid calculations of magnetohydrodynamic equilibria," J. Comput. Phys. **96**, 99–109 (1991).
[8] K. Watanabe, S. Sakakibara, Y. Narushima, H. Funaba, K. Narihara, K. Tanaka, T. Yamaguchi, K. Toi, S. Ohdachi, O. Kaneko *et al.*, "Effects of global MHD instability on operational high beta-regime in LHD," Nucl. Fusion **45**, 1247 (2005).
[9] S. Ohdachi, K. Watanabe, and S. Sakakibara, "Two approaches to the reactor-relevant high-beta plasmas with profile control in the large helical device," Tech. Rep. No. INIS-XA-08N0893; EX/8-1Rb (National Institute for Fusion Science, 2008), see https://www.osti.gov/etdeweb/biblio/21106531.
[10] H. Yamada, "Overview of results from the large helical device," Nucl. Fusion **51**, 094021 (2011).
[11] Y. Zhou, N. Ferraro, S. Jardin, and H. Strauss, "Approach to nonlinear magnetohydrodynamic simulations in stellarator geometry," Nucl. Fusion **61**, 086015 (2021).
[12] N. Nikulsin, R. Ramasamy, M. Hoelzl, F. Hindenlang, E. Strumberger, K. Lackner, S. Günter, and J. Team, "JOREK3D: An extension of the JOREK nonlinear MHD code to stellarators," Phys. Plasmas **29**, 063901 (2022).
[13] S. Patil and C. Sovinec, "Updates on numerical implementation and testing of NIMSTELL," in APS Division of Plasma Physics Meeting Abstracts (2023), pp. GP11–116.
[14] Y. Todo, N. Nakajima, M. Sato, and H. Miura, "Simulation study of ballooning modes in the large helical device," Plasma Fusion Res. **5**, S2062–S2062 (2010).

[15]Y. Zhou, K. Aleynikova, and N. M. Ferraro, "Nonlinear magnetohydrodynamic modeling of current-drive-induced sawtooth-like crashes in the w7-x stellarator," Phys. Plasmas **30**, 032503 (2023).
[16]A. Wright and N. Ferraro, "Investigating nonlinear magnetohydrodynamics in an optimized, reactor-scale quasi-axisymmetric stellarator," Phys. Plasmas **31**, 082509 (2024).
[17]A. Wright, P. Kim, N. Ferraro, and S. Hudson, "Modelling the nonlinear plasma response to externally applied three-dimensional fields with the stepped pressure equilibrium code," J. Plasma Phys. **88**, 905880508 (2022).
[18]H. Funaba, K. Watanabe, S. Sakakibara, S. Murakami, I. Yamada, K. Narihara, K. Tanaka, T. Tokuzawa, M. Osakabe, Y. Narushima *et al.*, "Local transport property of high-beta plasmas on LHD," Fusion Sci. Technol. **58**, 141–149 (2010).
[19]K. Nagaoka, H. Takahashi, M. Nakata, S. Satake, K. Tanaka, K. Mukai, M. Yokoyama, H. Nakano, S. Murakami, K. Ida *et al.*, "Transport characteristics of deuterium and hydrogen plasmas with ion internal transport barrier in the large helical device," Nucl. Fusion **59**, 106002 (2019).
[20]T. S. Hahm and R. M. Kulsrud, "Forced magnetic reconnection," Phys. Fluids **28**, 2412–2418 (1985).
[21]S. Futatani and Y. Suzuki, "Non-linear magnetohydrodynamic simulations of plasma instabilities from pellet injection in large helical device plasma," Plasma Phys. Controlled Fusion **61**, 095014 (2019).
[22]K. Ichiguchi, Y. Suzuki, M. Sato, Y. Todo, T. Nicolas, S. Sakakibara, S. Ohdachi, Y. Narushima, and B. Carreras, "Three-dimensional MHD analysis of heliotron plasma with RMP," Nucl. Fusion **55**, 073023 (2015).
[23]N. Mizuguchi, Y. Suzuki, and N. Ohyabu, "Nonlinear dynamics of a collapse phenomenon in heliotron plasma with large pressure gradient," Nucl. Fusion **49**, 095023 (2009).
[24]S. Ohdachi, K. Watanabe, K. Tanaka, Y. Suzuki, Y. Takemura, S. Sakakibara, X. Du, T. Bando, Y. Narushima, R. Sakamoto *et al.*, "Observation of the ballooning mode that limits the operation space of the high-density super-dense-core plasma in the LHD," Nucl. Fusion **57**, 066042 (2017).
[25]Y. Zhou, K. Aleynikova, C. Liu, and N. Ferraro, "Robustness of high-β w7-x plasmas against ideal ballooning instability," arXiv:2404.01966 (2024).
[26]R. Ramasamy, K. Aleynikova, N. Nikulsin, F. Hindenlang, I. Holod, E. Strumberger, and M. Hölzl, "Nonlinear MHD modeling of soft β limits in W7-AS," Nucl. Fusion **64**, 086030 (2024).